OPEN ACCESS
OPUS AUGSBURG

Universität Augsburg
Universitätsbibliothek

Measurement of strain, strain rate and crack evolution in shear cutting

Christoph Hartmann, Hannes Alois Weiss, Philipp Lechner, Wolfram Volk, Sebastian Neumayer, Jan Henrik Fitschen, Gabriele Steidl

Angaben zur Veröffentlichung / Publication details:

Hartmann, Christoph, Hannes Alois Weiss, Philipp Lechner, Wolfram Volk, Sebastian Neumayer, Jan Henrik Fitschen, and Gabriele Steidl. 2021. "Measurement of strain, strain rate and crack evolution in shear cutting." *Journal of Materials Processing Technology* 288 (August): 116872. https://doi.org/10.1016/j.jmatprotec.2020.116872.

Nutzungsbedingungen / Terms of use: **CC BY-NC-ND 4.0**

Dieses Dokument wird unter folgenden Bedingungen zur Verfügung gestellt: / This document is made available under these conditions:
CC-BY-NC-ND 4.0: Creative Commons: Namensnennung - Nicht kommerziell - Keine Bearbeitung
Weitere Informationen finden Sie unter: / For more information see:
https://creativecommons.org/licenses/by-nc-nd/4.0/deed.de

Measurement of strain, strain rate and crack evolution in shear cutting

Christoph Hartmann[a,*], Hannes Alois Weiss[a], Philipp Lechner[a], Wolfram Volk[a], Sebastian Neumayer[b], Jan Henrik Fitschen[b], Gabriele Steidl[b]

[a] Technical University of Munich, Chair of Metal Forming and Casting, Walther-Meissner-Strasse 4, 85748 Garching, Germany
[b] TU Kaiserslautern, Department of Mathematics, Paul-Ehrlich-Strasse 31, 67663 Kaiserslautern, Germany

1. Introduction

In shear cutting, the cutting surface formation is an important quality feature of the process. The cutting surface is mainly characterized by rollover, clean-shear share, fracture share and burr. Usually, the cutting line geometry and the component material to be used are predetermined and requirements on cutting surface quality are posed, such as low burr height or high clean-shear share. Three main parameters, the die clearance, the two cutting edge radii (die and punch) and the punch speed, play a central role in influencing the cutting surface of a component. In industrial practice, the determination of process parameters for manufacturing a predetermined cutting surface is an experience-based trial-and-error iterative process. Fig. 1 shows a fine-blanked component before and after process parameter optimization.

To address this issue, numerical methods, such as finite element analysis, are used when designing and analyzing the shear cutting process. Since state of the art numerical and experimental results often lack comparability or contradict each other, enhanced methods are needed to validate and verify the deployed material and numerical models. Therefore, the aim of this paper is to present an experimental setup for in situ strain and strain rate detection while maintaining the real-process boundary conditions. To this end, we also apply the optical flow approach with total generalized variation (TGV) prior introduced by Balle et al. (2019) to resolve the crack initiation and propagation during shear cutting.

2. State of the art

The die clearance is one of the most important process parameters for adjusting the desired cutting surface quality. Mori et al. (2010) points out that an increase in die clearance, for example, decreases the clean-shear share. As discussed by Schenk et al. (1978), the burr height can be influenced by cutting edge preparation and increases with increasing cutting edge wear. Itoh et al. (1987) observed that changing the cutting speed has a considerable influence on the ratio of clean-shear share to fracture share of the cutting surface due to the strain-rate-dependent properties of metallic materials.

Properties of metallic materials are mainly driven by the variables strain and strain rate and are dependent on the prevailing stress state. Bai and Wierzbicki (2009) discuss this topic in detail with respect to ductile fracture using the Mohr-Coulomb criterion. The influence of strain on the material behavior during a shear cutting process has already formed the subject of several experimental and numerical investigations. Where the real-process settings are concerned, the strain

* Corresponding author.
E-mail address: christoph.hartmann@utg.de (C. Hartmann).

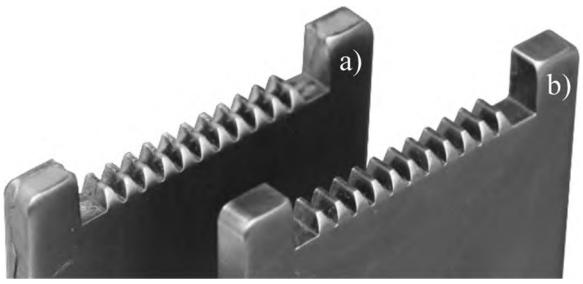

Fig. 1. Cutting surfaces before (a) and after (b) process parameter optimization for a fine-blanked component.

rate is only focused on in numerical work, such as by Vaz and Bressan (2002) or Subramonian et al. (2013) using finite element analysis. The calculations of Subramonian et al. (2013) predicted a strain rate of $10\,s^{-1}$ for a punch speed of 20 mm/s. Vaz and Bressan (2002) simulated the shear cutting process and concluded that the strain rate reaches about $19.000\,s^{-1}$ at a punch speed of 750 mm/s.

In his investigations, Timmerbeil (1957) has already shown that strains in the shear zone at the sheet edge can be measured ex situ using grid lines. He also describes the effects of strain on the cutting surface shape. Leung et al. (2004) present a square grid based system to measure severe and localized plastic deformations and apply it to shear cutting. Stegeman et al. (1999) as well as Wang and Wierzbicki (2015) use an optical measurement system to record the deformation during the process, which allows to determine the strain in the shear zone experimentally. The images, they recorded, are automatically evaluated using image correlation. Wang and Wierzbicki (2015) used the results to validate numerical results from finite element analysis. However, Timmerbeil (1957), Stegeman et al. (1999), and Wang and Wierzbicki (2015) measure the material strain at the open sheet edge. Due to the different three-dimensional stress states in regions closer to and along the cutting edge, the measured strain state at an open sheet edge does not correspond to a strain state in regions of the sheet that are farther away from the edge. Takahashi and Aoki (1996) circumvent this problem by utilizing lateral glass stops that prevent bulging of the sheet metal sample and should maintain a plain strain state across the entire cutting line. Aoki and Takahashi (2003) used the proposed setup to study the material flow for fine blanking setups using fourier phase transformation. Later, Sasada and Togashi (2014) fall back on the setup of Takahashi and Aoki (1996) and tracked the development of rollover during double-sided shear cutting. Nevertheless, a detailed analysis is missing, if the boundary condition actually remains constant along the whole cutting line. Hence, they still rely on the assumption that the strain and stress state are constant.

3. Problem formulation

Johnson and Cook (1985) observed that strain and strain rate drive both material and failure behavior. Material parameters used for shear cutting simulations are often determined utilizing tensile or compression tests, which are common for parameter identification in forming simulation. (For example Banabic et al. (2000) present an extensive collection of models for sheet metal forming simulation.) In contrast to the working direction of the shear cutting process, these tests operate in the sheet metal plane and a direct transfer of the results is therefore difficult.

Modelling material failure is a key aspect of numerical shear cutting process analysis. The model parameters required for describing the failure points are usually determined from a multitude of experiments in the sheet plane. Bai and Wierzbicki (2009) show a collection of test to adequately describe their Mohr-Coulomb fracture model. However, to describe the simulated process correctly, it would be necessary to use input parameters determined in a process-like experiment perpendicular to the sheet plane. With a similar aim for material characterization for machining, Shatla et al. (2001) proposed a two-dimensional orthogonal slot milling experiment that give enhanced results compared to Split-Hopkinson bar experiments.

In the state of the art, no measurement concept or system allows simultaneous recording of the main influencing parameters on the workpiece material as a function of predetermined process variables (punch speed, die clearance, cutting edge preparation) during chipless separation in the shear zone perpendicular to the sheet plane. The influences of strain and strain rate in the shear affected zone and their effect on the cutting surface have separately been considered detached from each other or ex situ, such as by Li, (2003), for example. An overall in situ measurement of the material-influencing state variables has not yet been carried out but is essential because their interaction strongly influences the mechanical behavior of the selected material in the shear affected zone. Crack formation plays an important role in damage and fracture modeling, however, we are not aware of any approach whose aim is to observe cracking during shear cutting.

The focus of our research lies on measuring the strain and strain rate distribution, and investigating the crack initiation and propagation during shear cutting perpendicular to the sheet plane.

4. Approach and setup

Our aim is to provide an experimental setup for quantitative observation of the material behavior in the shear affected zone, which may serve as a basis for material modeling and numerical analysis validation. For this purpose, a shear cutting tool is developed, which allows in situ high-resolution measurement of the occurring local strains and strain rates. Two main issues arise in respect of the implementation of the proposed experimental setup: the design of a suitable shear cutting tool that preserves plain strain conditions and the integration of a high resolution measurement systems with suitable data evaluation for observing the material behavior.

4.1. Experimental setup

The following descriptions of the shear cutting tool concern a closed cutting line, as for example present in piercing. A symmetric boundary condition exists when using a single sheet metal sample in the tool. Of course, the proposed experimental setup can also emulate an open cutting line by using two separate sheet metal samples on each side of the die (no connection under the punch), such as for trimming. The symmetry of the boundary conditions no longer holds for this open cutting line setup. Fig. 2 shows the shear cutting tool assembly.

A die set having two guide pillars serves as the basis for our testing tool. The guide pillars guarantee the positioning of the punch throughout the shear cutting process. For the shear cutting experiments the clearance between punch and die is maintained constant at 0.2 mm (5% relative clearance). Also the cutting edge geometries are not varied and remained constant for all tests with edge radii of 50 µm. In addition, a blank holder is used to fix the sheet metal in place on the die to prevent bending.

During the shear cutting operation, the lower tool is mounted on the press table while the upper tool is connected to the test bench's ram which applies the vertical force needed for the separation process. The universal test bench (Zwick-Roell Z150 TL) is used. The applied force is measured using a load cell mounted to the ram at the transverse of the universal test bench with a recording frequency of 1 kHz. The ram speed and hence the punching speed is controllable and set to 10 mm/s for the tests.

In this investigation, the testing tool's main task is to provide plain strain conditions during the in situ measurement. Stops on both sides of the cutting line prevent the expansion of the sheet metal in the z-direction. As a result, a three-dimensional stress state arises in contrast to the plain stress state of an open sheet edge. This stress state is

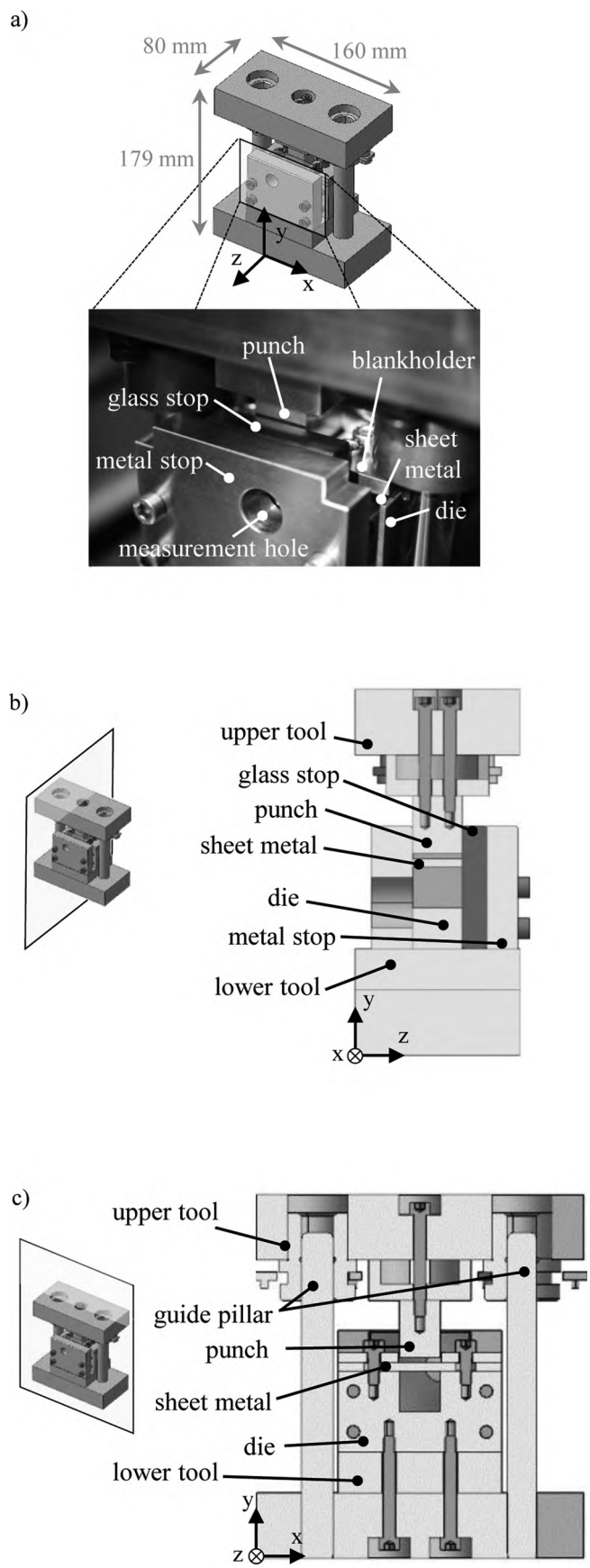

Fig. 2. (a) Assembly of the shear cutting tool with detailed view of the real shear cutting tool setup with glass stop. (b) Section of the shear cutting tool in the *y*-*z*-plane. (c) Section of the shear cutting tool in the *x*-*y*-plane.

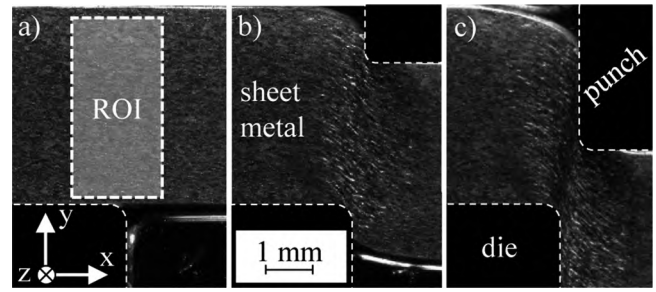

Fig. 3. Three selected stages of a shear cutting experiment at different time steps (a) to (c). In image (a), the region of interest (ROI) for the deformation analysis is included.

comparable to that in the shear zone along the cutting line.

One stop, which is in contact with the sheet metal, is made of glass and supported by a metal stop to ensure suitable stiffness of the testing tool. The in situ deformation observation is possible through a measurement hole in the metal stop, see Fig. 3 for some example views.

A high-speed camera (IDT Os3-S2) with magnification optics (*x* 12.5) is used for deformation recording. The optical data is provided as 8-bit grey scale images. Furthermore, a macro cold light source (Storz 300 W) is used for illumination. A typical view using the described experimental setup with a camera recording frequency of 5 kHz is shown in Fig. 3 for three different time steps. Fig. 3(a) displays the region of interest (ROI) for the observation. In the presented investigations, the ROI contains 220 × 800 pixels, which results in a pixel edge length of 4.3 µm. It is worth noting that all observations and analysis approaches work without any artificial speckle patterns. The latter are quite common especially in solid mechanics experiments. Leung et al. (2004) build their entire process strain measurement system on an artificial square grid. Also Wang and Wierzbicki (2015) prepare their samples using airbrush paint, which transmits the deformation information from the material. Unfortunately, for very large deformations, the paint is no longer a good transmitter of deformation, because it exhibits different material behavior. Using paint in combination with the glass stop is impossible because the paint would smear during the high deformations, resulting in errors and thus preventing a meaningful evaluation. In our analysis, we use the natural structure of the sheet metal material, which results from the grinding of the samples.

4.2. Sheet metal material

The material used for the experiments was an S355MC steel with thickness of 4.00 mm and width of 24.00 mm in the *z*-direction. The length of the sheet specimen is 100 mm. Our measurements of the classical mechanical properties are listed in Table 1, respectively.

4.3. Plain strain condition

Aoki and Takahashi (2003) introduce a tempered glass stop in shear cutting experiments to ensure a plain strain state and a three-dimensional stress state along the cutting line. However, a proof that the strain and stress state are constant is not given. This is addressed in this work. The shear cutting surface without a glass stop shows a clear

Table 1
Mechanical parameters of the steel sheet metal S355MC; YP: yield point, UTS: Ultimate tensile strength, MUE: Maximum uniform elongation, MH: Microhardness.

YP	UTS	MUE	MH
420 MPa	480 MPa	13%	174 HV

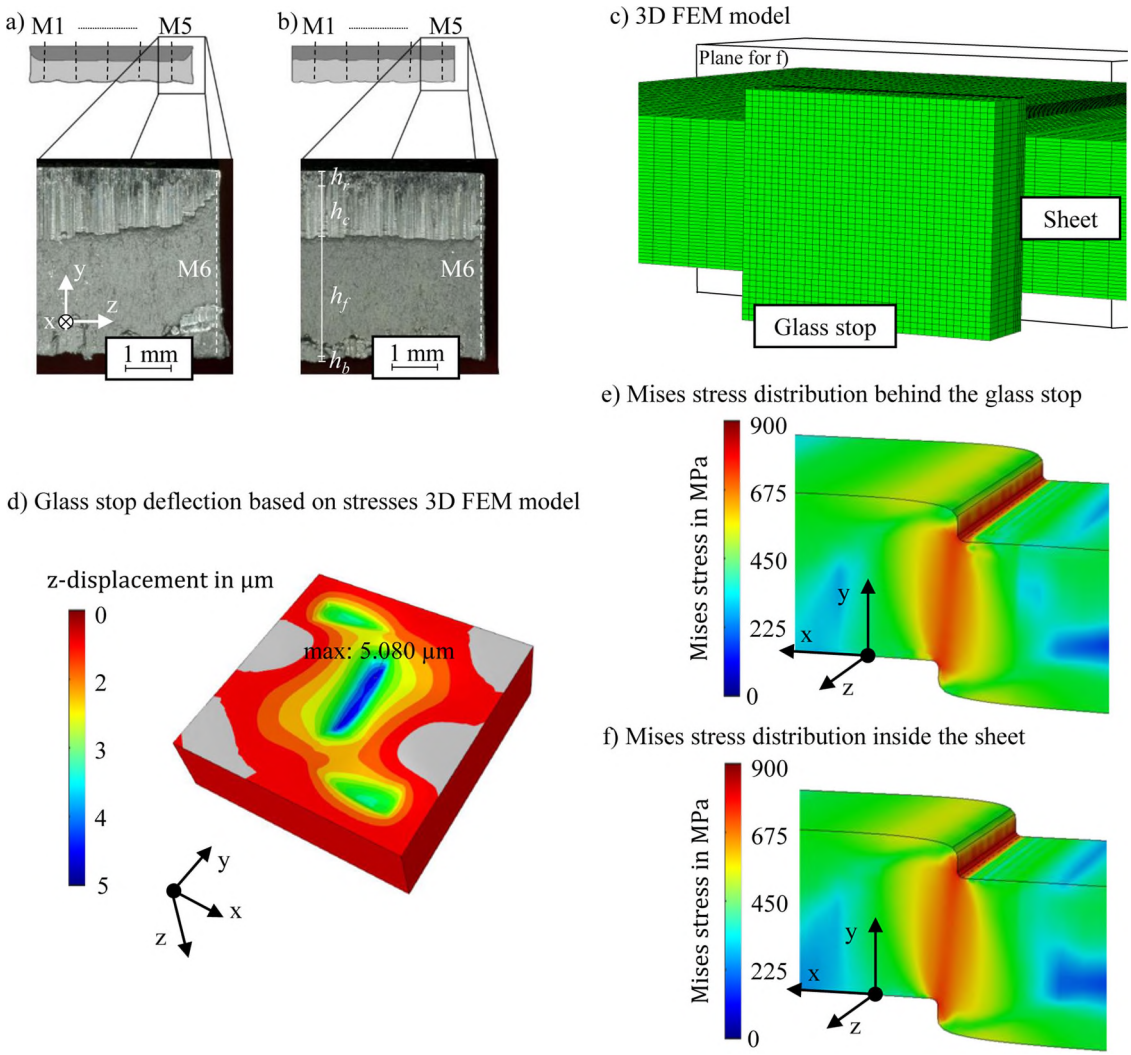

Fig. 4. Plane strain condition validation. Microscopic images of the shear cutting surface (a) without and (b) with a glass plate. M1 to M5 show the measurement locations for the characterization of the cutting surface. M6 represents the measurement location at the sheet metal edge. (c) Sheet and glass stop in the three-dimensional shear cutting simulation model. (d) Simulated glass stop deflection during shear cutting. Mises stress state in the observation plane (e) and inside the sheet material (f).

reduction of the clean shear towards the sheet metal edge, as shown in Fig. 4(a). If the elongation is limited by a stop, a constant ratio of the clean shear share to fracture share is formed along the entire cutting line, as seen in Fig. 4(b). This shows that both the strain distribution and the stress distribution along the cutting line are approximately constant.

To quantify the visual results, we measured the geometry of the cutting surface using a tactile system (Mahr Typ PCV 200). Five measurement locations within the sheet metal (M1 to M5 in Fig. 4) and one directly (distance of 0.01 mm) at the sheet metal edge (M6 in Fig. 4) have been considered. As discussed by the VDI-Fachbereich Produktionstechnik und Fertigungsverfahren (1994), a cutting surface may be characterized by its rollover height h_r, clean shear height h_c, fracture height and burr height h_b. The first three values are commonly expressed as a percentage of the sheet metal thickness. Table 2 summarizes the average values of the cutting surface properties for three samples measured at the six positions.

Using the glass stop, the geometry directly at the edge lies within the range of the measured geometries inside the sheet metal (listed in Table 2). Shear cutting without the glass stop leads to completely different cutting surface characteristics. Tests were also carried out with different degrees of lubrication to estimate the influence of friction

Table 2
Cutting surface characteristics in average of five samples at five measurement locations M1 to M5 in the sheet metal and M6 at the sheet metal edge for experiments with and without the glass stop. The notation is (value) ± (standard deviation).

Measurements	h_r	h_c	h_f	h_b
M1-5 glass	10 ± 1%	32 ± 2%	58 ± 2%	31 ± 2 µm
M1-5 no glass	11 ± 1%	33 ± 1%	56 ± 2%	34 ± 3 µm
M6 glass	9 ± 1%	31 ± 2%	60 ± 1%	30 ± 1 µm
M6 no glass	5 ± 2%	8 ± 3%	87 ± 3%	19 ± 3 µm

between the sheet metal and the stop. Regardless of the lubrication system used, respective cutting surfaces did not deviate from each other by more than the standard deviations given in Table 2.

To further support the experimental measurements, we set up a numerical model to study the glass stop deflection and the stress state in the observation plane compared to the stress state inside the material. Here, the numerical analysis serves as an additional, complementary, and qualitative tool for examining the proposed plane strain boundary condition. The FEM is utilized to support the experimental findings presented in Table 2. The three-dimensional model contains all main components of the experimental setup: blank holder, die, punch, sheet

metal, and glass stop. Fig. 4(c) shows the arrangement of the sheet and the glass stop in the FEM model (ABAQUS 2018). We set up the glass as pure elastic with a density of 2600 kg/m^3, Young's modulus of 70 GPa, and Possion's ratio of 0.22. As proposed by Buckley (1973), Friction between glass and steel sheet is modeled by Coulomb friction with $\mu = 0.5$. The elastic and visco-plastic constitutive model for the S355MC sheet metal is similar to the one used by Demmel (2014) and by Hörmann (2008). Fig. 4(d) shows that the maximum deflection of the glass stop is $\sim 5\,\mu$m, lying within the manufacturing tolerances of the experimental setup and the glass flatness. The Mises stress distributions in the shear zone are almost constant along the cutting line, as Fig. 4(e) and (f) indicate.

5. Evaluation methods

We combine two different approaches to evaluate high-speed images. The deformation evaluation is based on a classical block matching scheme, which is adapted to the large number of images provided from the high-speed imaging. The method is briefly discussed in Section 5.1. In Section 5.2 the concept of equivalent strain is introduced for visualization purposes. The crack evaluation uses an optical flow model with TGV prior introduced by Balle et al. (2019), which is described in Section 5.3.

The general problem framework in any kind of motion analysis is as follows: For gray-valued images $I_0, I_1\colon \mathbb{R}^2 \supset \Omega \to \mathbb{R}$ we are interested in the flow field $u = (u_1, u_2)\colon \Omega \to \mathbb{R}^2$ which describes how I_0 transforms into I_1. The term flow field is frequently used in the discussion of optical flow fields and is also reffered to as displacement field in block matching. In practice, our images $I_0, I_1\colon \mathcal{G} \to \mathbb{R}$ are defined on a two-dimensional rectangular grid $\mathcal{G} := \{1, \ldots, N_1\} \times \{1, \ldots, N_2\}$ and the same holds for the computed flow fields. Various different approaches for obtaining such flow fields are discussed throughout this section.

5.1. Deformation evaluation

We use a classical block matching method, namely digital image correlation, for the deformation evaluation. Digital image correlation has established itself as the default method for deformation analysis in experimental mechanics of solids. It relies on image merging algorithms (maximum search) based on correlation functions $C(u)\colon \eta \to \mathbb{R}^+$ in a predefined region $\eta \subset \Omega \subset \mathbb{R}^2$, for which Yamaguchi (1981) established the theoretical foundations. Peters and Ranson (1982) proposed that according to the registration, relative displacements $u(\boldsymbol{x})$ may be calculated between pixels $\boldsymbol{x} = (x, y)$ in a reference image I_0 and a skewed image I_1. To achieve sub-pixel resolutions, Pan et al. (2009) use data interpolation methods. In this paper, we utilize the zero-mean-normalized sum of squared difference criteria with affine warping proposed by Pan et al. (2013) that reads

$$C(u) = \int_\eta \left(\frac{I_0 - I_{m0}}{\Delta I_0} - \frac{I_1(u) - I_{m1}(u)}{\Delta I_1(u)} \right)^2 \mathrm{d}\boldsymbol{x}, \tag{1}$$

where $\Delta I_i^2(u) = \int_\eta (I_i(u) - I_{\mathrm{mi}}(u))^2\,\mathrm{d}\boldsymbol{x}$ and $I_{\mathrm{mi}}(u) = \frac{1}{|\eta|}\int_\eta I_i(u)\,\mathrm{d}\boldsymbol{x}$. Here, $I_1(u)$ describes the deformed image I_1 and because I_0 is not deformed, the bracket notation is omitted. The reliability-guided digital image correlation (RG-DIC) introduced by Pan (2009) is applied, which was inspired by reliability-guided phase unwarping developed by Su and Chen (2004). The main difference between the reliability-guided and conventional methods lies in the calculation path and initial guess for the sub-pixel calculation regime. Conventional methods work well under the assumption of continuous deformation. Reliability guided routines are more appropriate for heterogeneous deformation analysis. In a second step, we use the inverse compositional Gauss-Newton algorithm of Baker and Matthews (2001), where the displacements are recovered from a displacement mapping function with warping parameters p. Algorithm 1 shows a very brief pseudo code of the routine. We refer to the analysis of Hartmann et al. (2018) for detailed information on the implementation, precision and accuracy of the algorithm. The discrete subsets η_i are chosen as patches of 20×20 pixels around the pixel $i \in \mathcal{G}$ and second order polynomial trial functions are used for sub-pixel calculations. This configuration proves robust and in the present case provides the best trade-off between resolution and signal reconstruction without the use of filters. The routine considers each pixel in $\mathcal{G}$ for the deformation estimation.

Algorithm 1. Digital image correlation core.

Input: Images I_0, I_1, n subsets η_i, gridstep g, warping parameter p
for $i = 1, 2, \ldots, n$ **do**
  1. Calculate integer pixel accuracy
  u_i = compute_ R G-DIC(I_0, I_1, η_i, g)
  2. Calculate sub-pixel accuracy
  u_i = compute _ icgn(I_0, I_1, η_i, u_i, p)
  Output: Displacement field u

In order to cope with the large number of images, we implemented an image handling routine built around the digital image correlation core of Algorithm 1. The main task of the handling routine is to reduce calculation time and error accumulation. The routine extracts certain images from the high volume image stack, recorded during the experiments with the high-speed camera, and uses them for the displacement calculations. Here, the image selection interval d between two images is adapted based on a displacement threshold δ and a displacement gradient threshold ε, which ensures that non-linearities in the motion are detected within a predetermined accuracy. Lastly, the recording frequency of the high-speed camera gives the overall resolution, corresponding to an image interval of $d = 1$. Algorithm 2 sketches the complete handling routine.

Algorithm 2. Image handling routine.

Input: Image stack $I = \{I^{(0)}, \ldots, I^{(n)}\}$, initial image interval d_0, displacement threshold δ, displacement gradient threshold ε
$i = 1$, $d = d_0$
while $i + d \le n + 1$ **do**
  $u^{(i-1)} \longleftarrow$ result of Algorithm 1 for $I_0 = I^{(i-1)}$ and $I_1 = I^{(i-1+d)}$
  if $\max(||u^{(i-1)}||_2) \le \delta \wedge \max(||\nabla u^{(i-1)}||_2) \le \varepsilon$ **then**
    $i = i - 1 + d$
  else if $d > 2$ **then**
    $d = \mathrm{ceil}(d/2)$
  else
    $d = 1$, $i = i + 1$
Output: Stack of displacement fields $u = \{u^{(0)}, u^{(1)}, \ldots\}$

5.2. Equivalent strain

In continuum mechanics, measured strains are representative of the deformation. Motion is described through the displacement field and contains rigid body translations and rotations. Strains extract deformation information from the motion excluding all rigid body motions. In the conducted study, we utilize the equivalent strain measure proposed by Butcher and Abedini (2017), which is calculated solely based on the first principle component of the strain tensor and suited to shear dominated deformation

$$\varepsilon_{\mathrm{eq}} = \int \dot{\varepsilon}_{\mathrm{eq}}\,\mathrm{d}t \approx \sum \sqrt{\frac{2}{3}}\,\sinh(\mathrm{d}\varepsilon_1), \tag{2}$$

where $\mathrm{d}\varepsilon_1$ is the principle strain increment. Further, the von Mises equivalent strain $\varepsilon_{eq,2}$ serves as a local measure of deformation for the visualization of the cracking

$$\varepsilon_{\mathrm{eq},2} = \int \dot{\varepsilon}_{\mathrm{eq},2}\,\mathrm{d}t \approx \sum \sqrt{\frac{2}{3}(\mathrm{d}\varepsilon_{\mathrm{xx}}^2 + \mathrm{d}\varepsilon_{\mathrm{yy}}^2 + 2\,\mathrm{d}\varepsilon_{\mathrm{xy}}^2)}, \tag{3}$$

where $\mathrm{d}\varepsilon_{xx} = \frac{\partial \mathrm{d}u_1}{\partial x}$, $\mathrm{d}\varepsilon_{yy} = \frac{\partial \mathrm{d}u_2}{\partial y}$, $\mathrm{d}\varepsilon_{xy} = \frac{1}{2}\left(\frac{\partial \mathrm{d}u_1}{\partial x} + \frac{\partial \mathrm{d}u_2}{\partial x}\right)$ are the spatial strain increments.

Numerical computation of the gradients based on finite differences often results in accuracy problems. Hence, filters are often used to overcome this problem, but capturing details such as cracks is difficult or even impossible with this approach. Therefore, a more sophisticated approach is required.

5.3. Crack evaluation

The previous, correlation-based approach is well suited for analyzing experiments in which the deformation is mostly elastic-plastic and no cracks occur. Unfortunately, such methods are of limited use as soon as cracks evolve. Due to the window-based approach it is impossible to resolve local phenomena good enough and results are often too smooth. Here, we propose to apply the variational model introduced by some of the authors in Balle et al. (2019) for computing deformation and strain. In order to keep this paper self contained, we briefly sketch the method.

A variational model consists of two parts, a data term modeling how well the deformation field u fits to the given input images, and a regularizer containing prior knowledge about deformation and strain. Then, the displacement u is computed as a minimizer of an energy functional

$$\arg\min_u E(u) = E_{\text{data}}(u) + E_{\text{reg}}(u). \tag{4}$$

For our application, we choose a data term based on the common so-called *gray-value constancy* assumption, i.e., the gray values in the images are only displaced without changing them

$$I_0(x) - I_1(x + u(x)) = I_0(x) - I_1(x + u_1(x), y + u_2(x)) \approx 0.$$

Compared to the image correlation approach in (1), this can be seen as a window limited to a single pixel and skipping the normalization.

To make this equation assessable, it is linearized around some initial optical flow field $\bar{u}$ leading to

$$I_1(x + u(x)) \approx I_1(x + \bar{u}(x)) + \langle \begin{pmatrix} \partial_x I_1 \\ \partial_y I_1 \end{pmatrix}(x + \bar{u}(x)), u(x) - \bar{u}(x)\rangle. \tag{5}$$

Applying the L_1-norm, which is known to reduce the influence of outliers, results in the data term

$$E_{\text{data}}(u) = \|I_0(x) - I_1(x + \bar{u}(x)) - \langle \begin{pmatrix} \partial_x I_1(x + \bar{u}(x)) \\ \partial_y I_1(x + \bar{u}(x)) \end{pmatrix}, u(x) - \bar{u}(x)\rangle\|_1.$$

For crack analysis, the regularizer choice is the crucial part of the model. In the proposed approach, the basic idea is to split the strain ∇u into two components $\tilde{a}$ and a. The first component represents the cracks and can have locally large values, while the second component expresses the smooth deformation. This enables us to evaluate cracks correctly without observing undesirably smooth results.

Modeling this idea mathematically, the first part of the strain is assumed to be sparse, so the Frobenius norm of the strain is used as a regularizer. The second part is assumed to be smoother, so that a first order derivative is chosen as a regularization term here. Combining both terms leads to the following regularizer

$$E_{\text{reg}}(u) = \text{TGV}(u) := \inf_{a+\tilde{a}=\nabla u} \left\{ \int_\Omega \lambda_1 \|\tilde{a}\|_F + \lambda_2 \|\nabla a\|_F \, \mathrm{d}x \right\} \tag{6}$$

$$= \inf_a \left\{ \int_\Omega \lambda_1 \|\nabla u - a\|_F + \lambda_2 \|\nabla a\|_F \, \mathrm{d}x \right\}, \tag{7}$$

which is the well known total generalized variation introduced by Bredies et al. (2010). A numerical comparison of different regularizers and their effects can be found in Balle et al. (2019).

Transferring the terms to the discrete setting leads to a convex, but non-smooth model for which Balle et al. (2019) have shown that a minimizer exists. This minimization problem can be solved efficiently using primal-dual algorithms from convex analysis, see Algorithm 3, where every update step has a closed-form solution. The notation in the algorithm is described in the discrete model outlined below. Note that the algorithm must be combined with common strategies for optical flow computation in order to cope with large displacements. More precisely, we apply a coarse-to-fine scheme and additional filtering steps as sketched in the pseudo-code in Algorithm 4. For our application in crack analysis, we use $j = 70$ scales, a scaling factor of $\rho = 0.97$, and a standard deviation of $\sigma = 0.3$. For further implementation details we refer to Balle et al. (2019).

Algorithm 3. Primal dual algorithm for optical flow and strain computation.

$$\begin{aligned}
u^{(r+1)} &= \arg\min_{u\in\mathbb{R}^{2N}} \left\{ \|(A\ B)u + c\|_1 + \frac{1}{2\tau_1}\|u - (u^{(r)} - \tau_1\tau_2\nabla^{\mathrm{T}}\bar{b}_1^{(r)})\|_2^2 \right\} \\
a^{(r+1)} &= a^{(r)} - \tau_1\tau_2(\tilde{\nabla}^{\mathrm{T}}\bar{b}_2^{(r)} - \bar{b}_1^{(r)}) \\
s^{(r+1)} &= \arg\min_{s\in\mathbb{R}^{4N}} \left\{ \lambda_1 \|s\|_{2,1} + \frac{\tau_2}{2}\|s - (b_1^{(r)} + \nabla u^{(r+1)} - a^{(r+1)})\|_2^2 \right\} \\
t^{(r+1)} &= \arg\min_{t\in\mathbb{R}^{6N}} \left\{ \lambda_2 \|t\|_{2,1} + \frac{\tau_2}{2}\|t - (b_2^{(r)} + \tilde{\nabla} a^{(r+1)})\|_2^2 \right\} \\
b_1^{(r+1)} &= b_1^{(r)} + \nabla u^{(r+1)} - a^{(r+1)} - s^{(r+1)} \\
b_2^{(r+1)} &= b_2^{(r)} + \tilde{\nabla} a^{(r+1)} - t^{(r+1)} \\
\bar{b}_1^{(r+1)} &= 2b_1^{(r+1)} - b_1^{(r)} \\
\bar{b}_2^{(r+1)} &= 2b_2^{(r+1)} - b_2^{(r+1)} - b_2^{(r)}
\end{aligned}$$

Initialization: $u^{(0)} = u_0 \in \mathbb{R}^{2N}$, $a^{(0)} = a_0 \in \mathbb{R}^{4N}$, $b_1^{(0)} = \mathbf{0} \in \mathbb{R}^{4N}$, $b_2^{(0)} = \mathbf{0} \in \mathbb{R}^{6N}$, $\bar{b}_1^{(0)} = \mathbf{0} \in \mathbb{R}^{4N}$, $\bar{b}_2^{(0)} = \mathbf{0} \in \mathbb{R}^{6N}$, $\tau_1 = \frac{1}{4}$, $\tau_2 = \frac{1}{4}$

for $r = 0, 1, \ldots$ **do**

$$\begin{aligned}
u^{(r+1)} &= \arg\min_{u\in\mathbb{R}^{2N}} \left\{ \|(A\ B)u + c\|_1 + \frac{1}{2\tau_1}\|u - (u^{(r)} - \tau_1\tau_2\nabla^{\mathrm{T}}\bar{b}_1^{(r)})\|_2^2 \right\} \\
a^{(r+1)} &= a^{(r)} - \tau_1\tau_2(\tilde{\nabla}^{\mathrm{T}}\bar{b}_2^{(r)} - \bar{b}_1^{(r)}) \\
s^{(r+1)} &= \arg\min_{s\in\mathbb{R}^{4N}} \left\{ \lambda_1 \|s\|_{2,1} + \frac{\tau_2}{2}\|s - (b_1^{(r)} + \nabla u^{(r+1)} - a^{(r+1)})\|_2^2 \right\} \\
t^{(r+1)} &= \arg\min_{t\in\mathbb{R}^{6N}} \left\{ \lambda_2 \|t\|_{2,1} + \frac{\tau_2}{2}\|t - (b_2^{(r)} + \tilde{\nabla} a^{(r+1)})\|_2^2 \right\} \\
b_1^{(r+1)} &= b_1^{(r)} + \nabla u^{(r+1)} - a^{(r+1)} - s^{(r+1)} \\
b_2^{(r+1)} &= b_2^{(r)} + \tilde{\nabla} a^{(r+1)} - t^{(r+1)} \\
\bar{b}_1^{(r+1)} &= 2b_1^{(r+1)} - b_1^{(r)} \\
\bar{b}_2^{(r+1)} &= 2b_2^{(r+1)} - b_2^{(r+1)} - b_2^{(r)}
\end{aligned}$$

Output: Strain components s, a and flow field u

Next, we recall the data term and the regularizer in the discrete model to clarify the notation in the algorithms. The data term reads as

$$E_{\text{data}}(u) = \|(A\ B)u + c\|_1 = \|Au_1 + Bu_2 + c\|_1, \tag{8}$$

with

$$A = \text{diag}(T_{\bar{u}}(\nabla_x I_1)), \quad B = \text{diag}(T_{\bar{u}}(\nabla_y I_1)), \tag{9}$$

$$c = -\text{diag}(T_{\bar{u}}(\nabla_x I_1))\bar{u}_1 - \text{diag}(T_{\bar{u}}(\nabla_y I_1))\bar{u}_2 + T_{\bar{u}} I_1 - I_0. \tag{10}$$

Here, the partial derivatives are replaced by forward differences ∇_x and ∇_y and $T_{\bar{u}} I$ denotes the evaluation of $I \circ \bar{u}$ at grid points based on bilinear interpolation. Using the mixed norm $\|f\|_{2,1}$ given by

$$\|f\|_{2,1} := \sum_{j\in\mathcal{G}} \|f(j)\|_2,$$

the TGV regularizer becomes

$$\mathrm{TGV}(u) = \min_{a}\{\lambda_1\|\nabla u - a\|_{2,1} + \lambda_2\|\tilde{\nabla} a\|_{2,1}\}, \tag{11}$$

where the gradients are defined as

$$\nabla := \begin{pmatrix} \nabla_x \\ \nabla_y \end{pmatrix}, \quad \tilde{\nabla} := \begin{pmatrix} \tilde{\nabla}_x \\ \frac{12}{(}\tilde{\nabla}_x + \tilde{\nabla}_y) \\ \tilde{\nabla}_y \end{pmatrix} \tag{12}$$

with backward differences $\tilde{\nabla}_x$, $\tilde{\nabla}_y$.

Finally, let us remark that Algorithm 3 computes the desired strain tensor $\varepsilon = a$ and the non smooth part s corresponding to cracks in the material directly within the iteration process and no subsequent computation of derivatives is required.

Algorithm 4. Coarse-to-fine scheme.

Input: Images I_0, I_1, number of levels j, scaling factor ρ, Gaussian kernel K_σ with standard deviation σ

1. Create image pyramid by downscaling and smoothing:

$I_0^{(0)} = I_0$, $I_1^{(0)} = I_1$

for $i = 1, 2, \ldots, j-1$ **do**

$I_0^{(i)} = I_0^{(i-1)} * K_\sigma$, $I_1^{(i)} = I_1^{(i-1)} * K_\sigma$

$I_0^{(i)} = \mathrm{resize}(I_0^{(i)}, \lceil \rho^i N_1 \rceil, \lceil \rho^i N_2 \rceil)$

$I_1^{(i)} = \mathrm{resize}(I_1^{(i)}, \lceil \rho^i N_1 \rceil, \lceil \rho^i N_2 \rceil)$

2. Start with 0 flow and compute flow on the coarsest level:

$u_0^{(j-1)} = \mathbf{0}$, $a_0^{(j-1)} = \mathbf{0}$

$[u^{(j-1)}, a^{(j-1)}] = \mathrm{compute_flow}(I_0^{(j-1)}, I_1^{(j-1)}, u_0^{(j-1)}, a_0^{(j-1)})$

$u^{(j-1)} = \mathrm{medfilt}(u^{(j-1)})$, $a^{(j-1)} = \mathrm{medfilt}(a^{(j-1)})$

3. Main part, go from coarse to fine and use flow from last level as initialization for computation on the next level:

for $i = j-2, j-3, \ldots, 0$ **do**

$u_0^{(i)} = \frac{\lceil \rho^i N_1 \rceil}{\lceil \rho^{i+1} N_1 \rceil}\mathrm{resize}(u^{(i+1)}, \lceil \rho^i N_1 \rceil, \lceil \rho^i N_2 \rceil)$

$a_0^{(i)} = \mathrm{resize}(a^{(i+1)}, \lceil \rho^i N_1 \rceil, \lceil \rho^i N_2 \rceil)$

$[u^{(i)}, a^{(i)}] = \mathrm{compute_flow}(I_0^{(i)}, I_1^{(i)}, u_0^{(i)}, a_0^{(i)})$

$u^{(i)} = \mathrm{medfilt}(u^{(i)})$, $a^{(i)} = \mathrm{medfilt}(a^{(i)})$

Output: Flow field $u^{(0)}$, smooth strain $a^{(0)}$

6. Results and discussion

The presented results are secured by five test executions with identical configuration of the shear cutting setup with a closed cutting line (symmetry boundary conditions in the tool). Fig. 5 shows the respective force-travel curves. In phase I the applied force increases steeply due to elastic deformation of all components within the force flow, as also, for example, Klingenberg and Singh (2005) noted in their analysis of the cutting force. At the transition from phase I to phase II the flow limit of the sheet metal material is reached and the plastic deformation of the material starts in phase II, as described by Hoffmann et al. (2012), p. 682. Due to the progressive deformation and the dominating hardening (strain hardening and strain rate hardening) of the sheet material, the applied force continues to increase. As the punch further penetrates the sheet metal, the cross section between the cutting edges decreases while the temperatures increase due to the plastic work dissipation. Combined, these effects result in a degressive force curve until the maximum applied force at point B is reached, which in average is 71.79 kN. At Point A hardening effects dominate, at point C softening effects predominate and point D denotes the transition between phase II and phase III, which represents the crack initiation and propagation phase. Cracks form and the sheet material is finally separated during phaseIII. In phase IV, the potential energy stored during elastic deformation from phase I to phase III is released in form of a cutting impact, which is described in detail by Hoffmann et al. (2012),p. 688. Due to the applied force measuring frequency of 1 kHz and the distance of the load cell from the punch, the cutting impact oscillation is smoothed. Hence, the applied force in phase IV only shows a regressive characteristic. The almost perfect agreement (standard deviation < 0.1 kN until the end of phase III) between the recorded experimental curves shows the reproducibility of the considered shear cutting experiments.

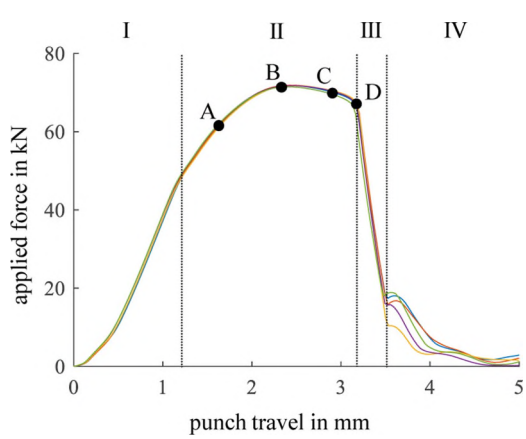

Fig. 5. Force-travel graphs for five shear cutting experiments.

6.1. Strain and strain rate analysis

The strain and strain rate analysis is based exclusively on the block matching-based image analysis presented in Section 5.1. The results focus on phase II of the force-travel curve in Fig. 5. For the evaluation, the defined region of interest around the shear zone is used. Digital image correlation, as described in Section 5.1, is utilized for the deformation analysis until crack initiation. Four characteristic stages throughout the deformation phase II are presented (Points A to D). In Fig. 6(a)–(h), the horizontal and vertical displacement fields and in Fig. 6(i)–(l) to the equivalent strain fields of the respective stages are shown. More precisely, Fig. 6(a), (e), and (i) show the corresponding states for point A in the force-travel curve from Fig. 5. Here, hardening effects dominate the deformation in the shear zone. The state at point B represents the point of maximum punch force and is shown in Fig. 6(b), (f), and (j). Point C is representative for softening dominated deformation and is shown in Fig. 6(c), (g), and (k). Finally, Fig. 6(d), (h), and (l) depict the states for point D, where the forming limit of the material is reached. Overall, the displacement fields show the expected progressions and a qualitative evaluation of the total motion of the experimental setup is possible. Note that the very low vertical displacements (almost zero) in the left half of the sheet metal show the high stiffness of the test setup.

Further, the equivalent strain fields visualize the development of the typical shear band deformation structure during shear cutting. The highest strains occur just behind the sheet metal surface at the cutting edges of the punch and the die. Using the median of 10 by 10 grids to suppress artifacts, a maximum equivalent strain value $\varepsilon_{eq} = 5.8$ has been detected in Fig. 6(l). In between these two points, a slight gradient towards the middle of the shear zone is visible. The largest strains appear at the punch side of the sheet metal, which is in good agreement with theoretical findings on shear cutting. For a summary on the theory see for example Hoffmann et al. (2012), p. 677–698. From point A to point C the localization of the deformation is amplified. Hardening effects can be seen as a homogenization driver smoothing out deformation until the softening effects become dominant at point B. From point B to point D via point C the localization of the deformation proceeds, driven mainly by the decreasing cross section (geometrical and damage-induced) and supported by the softening due to the temperature increase.

Fig. 7(a) shows the principle strain distribution in the region of interest for the conducted shear cutting experiment. Furthermore, the analog strain distribution for the identical test setup without glass stop

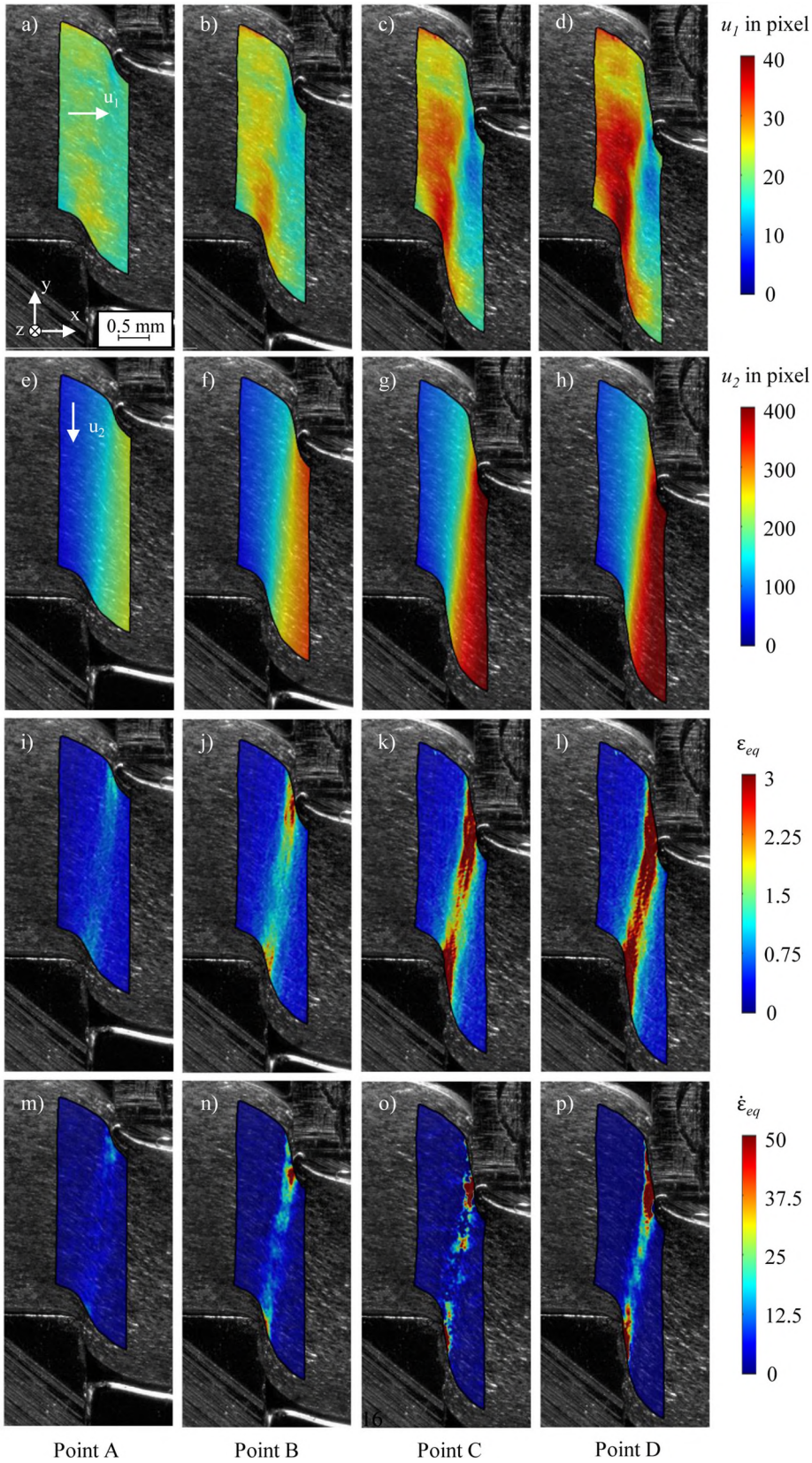

Fig. 6. Shear cutting displacement distributions (a)–(h), equivalent strain field (i)–(l), and equivalent strain rate field (m)–(p) at point A to D.

is shown. Both principle strain distributions are shown for 2.131 mm punch penetration, which is the point just before failure in the test without glass stop. Without the glass stop, deformation gets an additional degree of freedom perpendicular to the observation plane. The third principle strain may be no longer seen as approximately zero. This motion yields a reduction in the two first principle components shown in the diagram. The free surface also leads to reduced hydrostatic pressure in the shear zone, which promotes premature fracture

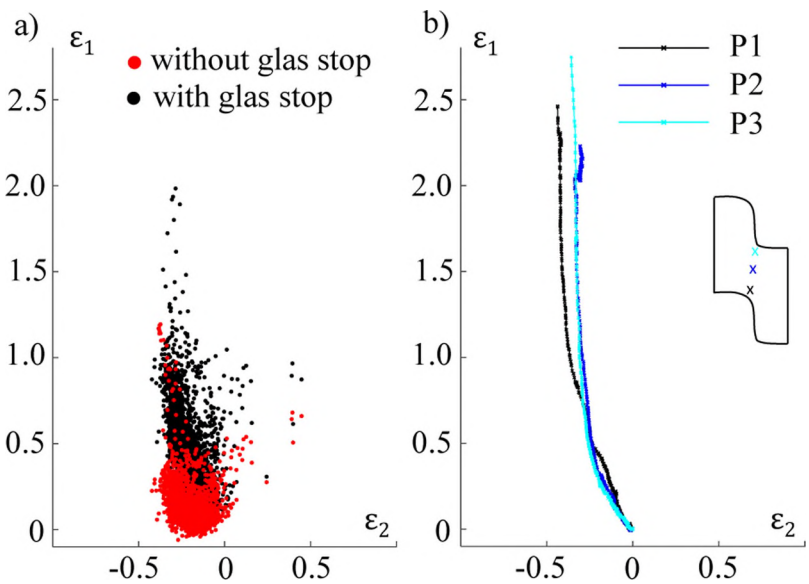

Fig. 7. (a) Principle strain distributions in the region of interest for a shear cutting experiment with glass stop and a shear cutting experiment without glass stop. The distributions are shown for the punch travel, where the test without glass stop shows earlier crack initiation. (b) This plot shows the strain paths of three different material points located in the shear zone. Please note that the diagrams may not be interpreted similar to the well-known pendant from sheet metal forming, the FLC, since deformation boundary conditions are different.

initiation.

Fig. 7(b) shows three selected strain paths for the shear cutting experiment with glass stop. The strain increments confirm that the thresholds in the deformation estimation routine, see Section 5.1, are effective to control their size. In all three paths, the first principle strain grows much faster compared to the second principle strain, indicating shear domination with ongoing deformation. The strain paths shown in Fig. 7(b) indicate that the deformation during shear cutting is non-proportional until fracture. Further, the strain paths allow statements to be made regarding local volume constancy. Assuming volume constancy, value pairs of $\varepsilon_1 \neq \varepsilon_2$ would inevitably require a strain component in x_3-direction. However, after initially maintaining volume constancy, the shear cutting process shows significant deviations from this. However, especially with progressive punch penetration and deformation, the local volume constancy no longer holds for the shear cutting process, since, for example, high pressures and damage to the material are to be included in the volume balance.

In Fig. 6(m)–(p), we display the respective strain rate distributions. The local strain rates are calculated using finite differences, which in our opinion is reasonable due to the high resolution in time and the small strain increments, see Fig. 8(b). Initially for points A and B in the force-travel curve, only moderate strain rates occur. At point B values up to $25\,\mathrm{s}^{-1}$ are reached. In Fig. 6(o) and (p), the local equivalent strain rates reach $50\,\mathrm{s}^{-1}$ in the shear zone. Compared to the strain distributions, the strain rate distributions appear less homogeneous. Note that the measured values lie within the same scale as the numerical predictions of Subramonian et al. (2013), with maxima next to the cutting edges.

6.2. Crack initiation and propagation

Our results for crack initiation and propagation combine the deformation evaluation presented in Section 5.1 and the TGV-based crack evaluation routine proposed in Section 5.3. When the material-dependent formability limit in the sheet metal between punch edge and die edge is reached, first cracks appear in the material. In the force-travel curve, see Fig. 5, this occurs in the transition between phase II and phase III (point D). Crack initiation is mainly influenced by the superposition of shear stresses, tensile stresses and compressive stresses in the shear zone, which vary depending on the process parameters. Timmerbeil (1957) states that if the cutting edges are equally sharp, cracking usually starts at the die. This is the point at which tensile and bending stresses should combine. The total stress along the sheet surface contacting the punch is lower as the tensile stresses in material flow direction are partially compensated by compressive stresses from the punch. This compressive state is clearly visible in our experiments, especially for the horizontal displacements in Fig. 6(c) and (d). Depending on the sheet metal material and the magnitude of the clearance, the crack may also be initiated at the punch. For a correct process setting, after initiation, the cracks from both cutting edges converge and finally result in a complete separation of the material at the end of phase III, as explained also by Hoffmann et al. (2012).

In Fig. 8, we show eight different stages of the shear cutting experiment during phase III in the force-travel curve. Fig. 8(a)–(c) represent the crack initiation process. Here, image (a) is the last stage of the deformation analysis, see Fig. 6(d), (h), (l), and (p). The images depict the classical equivalent strain measure $\varepsilon_{eq,2}$ to improve visibility of the crack, i.e., with better separation between smooth and non-smooth fields. Here, we prioritize visualization over physical consistency, since for cracks the strain loses its physical meaning anyways and serves purely as illustration of the crack propagation. Crack initiation starts between image (b) and (c), see also Fig. 6(i) and (j) for more details. We observe that the crack is initiated at the die, although higher equivalent strains appear on the punch edge. However, the superimposed compressive stresses prevent the crack initiation. Hence, the stress-based theoretical derivations and ex situ observations announced in the state of the art can be observed also in situ resolved in time.

Crack propagation is depicted in Fig. 6(d)–(h). In image (d) a crack also appears at the punch edge. Throughout the image sequence (e)–(h), the cracks converge, leading to the separation of the sheet metal, see Fig. 6(k)–(n) for a detailed view. Again, the ex situ observations and theoretical derivations described in the state of the art are confirmed by the in situ analysis. For our uniformly prepared cutting edge geometries, both cracks meet directly in the middle of the sheet metal, leading to uniform fracture share with absence of secondary clean-shear formation on the cutting surface.

7. Conclusion

In this paper, we propose an experimental setup and evaluation methodology for analyzing the shear cutting process. In contrast to previous investigations, our approach preserves the boundary values and is combined with high resolution optical measurements. No special sample preparation, such as the application of a speckle pattern, is necessary for digital image analysis. The setup and evaluation routine is

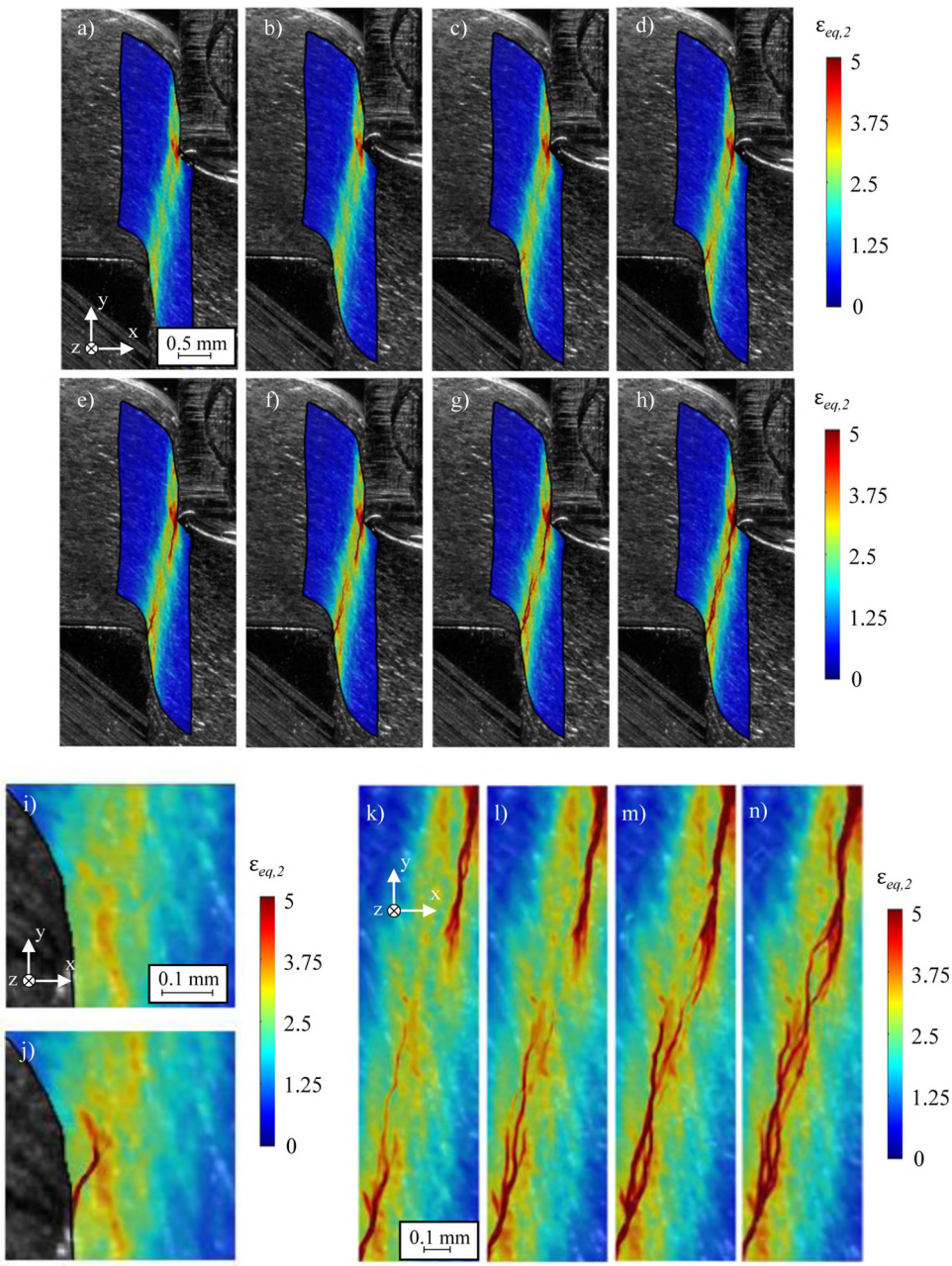

Fig. 8. Classical equivalent strain distributions during crack initiation, images (a)–(c), and propagation, images (d)–(h), for a shear cutting experiment. Image (i) and (j) represent the detailed views of the die edge in (b) and (c), respectively. Image (k)–(n) are detailed views of the shear zone in (e)–(h).

fully scalable and capable to handle various sheet thicknesses as long as the optics provide suitable magnification and the sheet metal edge texture provides sufficient grey scale contrast. Further, the proposed high-speed evaluation routine formed by a sequential combination of block matching and an optical flow model with TGV prior may also be used in a more general context for dynamic observations. Especially the resolution of cracking behaviour under plain strain boundary conditions offers enormous potential. An extension of the evaluation routine to three dimensions could further increase its scope.

The whole setup can be used to validate numerical analyses, which is used for process design. Currently, a validation is usually based on the final geometry of the cutting surface, without any consideration of the evolution of the strain fields or strain rate fields. The same applies to cracking. This is particularly interesting for the evaluation of material models used in numerical analyses as well as their parameter determination methods. Note that the setup operates at real-process speeds, which allows this kind of analysis. Finally, the proposed methodology is highly suited to inverse analysis of coupled elastic-plastic-damage models, as it provides local data that is highly resolved in space and time with constant boundary values throughout the duration of the process.

CRediT author statement

Christoph Hartmann: Conceptualization, Methodology, Software, Validation, Formal analysis, Investigation, Resources, Data Curation, Writing – Original Draft, Writing – Review & Editing, Visualization, Project Administration

Hannes Alois Weiss: Conceptualization, Validation, Writing – Review & Editing

Philipp Lechner: Writing – Review & Editing

Wolfram Volk: Writing – Review & Editing, Funding acquisition,

Supervision

Sebastian Neumayer: Software, Formal analysis, Writing – Original Draft, Writing – Review & Editing

Jan-Hendrik Fitschen: Software, Writing – Review & Editing

Gabriele Steidl: Writing – Review & Editing, Funding acquisition, Supervision

Conflicts of interest

None declared.

Declaration of Competing Interest

The authors report no declarations of interest.

Acknowledgments

The authors would like to thank the German Research Foundation (DFG) for financial support under grant number VO 1487/27 and within the RTG1932, project area P3.

References

Aoki, I., Takahashi, T., 2003. Material flow analysis on shearing process by applying Fourier phase correlation method: analysis of piercing and fine-blanking. J. Mater. Process. Technol. 134, 45–52. https://doi.org/10.1016/S0924-0136(02)00917-2.

Bai, Y., Wierzbicki, T., 2009. Application of extended mohr-coulomb criterion to ductile fracture. Int. J. Fract. 161, 1. https://doi.org/10.1007/s10704-009-9422-8.

Baker, S., Matthews, I., 2001. Equivalence and efficiency of image alignment algorithms. Proceedings of the 2001 IEEE Computer Society Conference on Computer Vision and Pattern Recognition. CVPR 2001 I. https://doi.org/10.1109/CVPR.2001.990652.

Balle, F., Beck, T., Eifler, D., Fitschen, J.H., Schuff, S., Steidl, G., 2019. Strain analysis by a total generalized variation regularized optical flow model. Inverse Probl. Sci. Eng. 27, 540–564. https://doi.org/10.1080/17415977.2018.1475479.

Banabic, D., Bunge, H., Pöhlandt, K., Tekkaya, A., 2000. Formability of Metallic Materials: Plastic Anisotropy, Formability Testing, Forming Limits. Engineering Materials. Springerhttps://doi.org/10.1007/978-3-662-04013-3.

Bredies, K., Kunisch, K., Pock, T., 2010. Total generalized variation. SIAM J. Imaging Sci. 3, 492–526. https://doi.org/10.1137/090769521.

Buckley, D., 1973. Friction Behavior of Glass and Metals in Contact with Glass in Various Environments. NASA Technical Note D-7529.

Butcher, C., Abedini, A., 2017. Shear confusion: identification of the appropriate equivalent strain in simple shear using the logarithmic strain measure. Int. J. Mech. Sci. 134, 273–283. https://doi.org/10.1016/j.ijmecsci.2017.10.005.

Demmel, P., 2014. In-Situ Temperature Measurement in Shear Cutting PhD Thesis. Technical University of Munich.

Hartmann, C., Wang, J., Opritescu, D., Volk, W., 2018. Implementation and evaluation of optical flow methods for two-dimensional deformation measurement in comparison to digital image correlation. Optics Lasers Eng. 107, 127–141. https://doi.org/10.1016/j.optlaseng.2018.03.021.

Hoffmann, H., Spur, G., Neugebauer, R., 2012. Handbuch Umformen. Edition Handbuch der Fertigungstechnik, 2nd ed. Carl Hanser Fachbuchverlaghttps://doi.org/10.3139/9783446430044.

Hörmann, F., 2008. Einfluss der Prozessparameter auf einstufige Scherschneidverfahrenzum Ausschneiden mit endkonturnaher Form PhD Thesis. Technical University of Munich.

Itoh, M., Yoshida, F., Inoue, M., Ohmori, M., 1987. Combined effects of hydrostatic pressure and punching speed on blanking behaviors of 2s-aluminum. Adv. Technol. Plast. 1, 307–312. https://doi.org/10.1016/j.jmatprotec.2009.11.014.

Johnson, G., Cook, W., 1985. Fracture characteristics of three metals subjected to various strains, strain rates, temperatures and pressures. Eng. Fract. Mech. 21, 31–48. https://doi.org/10.1016/0013-7944(85)90052-9.

Klingenberg, W., Singh, U., 2005. Comparison of two analytical models of blanking and proposal of a new model. Int. J. Mach. Tools Manuf. 45, 519–527. https://doi.org/10.1016/j.ijmachtools.2004.09.002.

Leung, Y., Chan, L., Tang, C., Lee, T., 2004. An effective process of strain measurement for severe and localized plastic deformation. Int. J. Mach. Tools Manuf. 44, 669–676. https://doi.org/10.1016/j.ijmachtools.2004.02.009.

Li, Ming, 2003. Sliver Generation Reduction in Trimming of Aluminum Autobody Sheet. J. Manuf. Sc. Eng. 125 (1), 128–137. https://doi.org/10.1115/1.1540113.

Mori, K.i., Abe, Y., Suzui, Y., 2010. Improvement of stretch flangeability of ultra high strength steel sheet by smoothing of sheared edge. J. Mater. Process. Technol. 210, 653–659. https://doi.org/10.1016/j.jmatprotec.2009.11.014.

Pan, B., 2009. Reliability-guided digital image correlation for image deformation measurement. Appl. Optics 48, 1535–1542. https://doi.org/10.1364/AO.48.001535.

Pan, B., Li, K., Tong, W., 2013. Fast, robust and accurate digital image correlation calculation without redundant computations. Exp. Mech. 53, 1277–1289. https://doi.org/10.1007/s11340-013-9717-6.

Pan, B., Qian, K., Xie, H., Asundi, A., 2009. Two-dimensional digital image correlation for in-plane displacement and strain measurement: a review. Meas. Sci. Technol. 20, 062001. https://doi.org/10.1088/0957-0233/20/6/062001.

Peters, W., Ranson, W., 1982. Digital imaging techniques in experimental stress analysis. Opt. Eng. 21, 427–431. https://doi.org/10.1117/12.7972925.

Sasada, M., Togashi, T., 2014. Measurement of rollover in double-sided shearing using image processing and influence of clearance. Proc. Eng. 81, 1139–1144. https://doi.org/10.1016/j.proeng.2014.10.248. 11th International Conference on Technology of Plasticity, ICTP 2014, 19–24 October 2014, Nagoya Congress Center, Nagoya, Japan.

Schenk, H., Prölss, E., Guenther, K., 1978. Blanking of sheet metal relationship between process conditions and fracture of cut edge. Ann. CIRP 27, 159.

Shatla, M., Kerk, C., Altan, T., 2001. Process modeling in machining. Part I: Determination of flow stress data. Int. J. Mach. Tools Manuf. 41, 1511–1534. https://doi.org/10.1016/S0890-6955(01)00016-5.

Stegeman, Y., Goijaerts, A., Brokken, D., Brekelmans, W., Govaert, L., Baaijens, F., 1999. An experimental and numerical study of a planar blanking process. J. Mater. Process. Technol. 87, 266–276. https://doi.org/10.1016/S0924-0136(98)00362-8.

Su, X., Chen, W., 2004. Reliability-guided phase unwrapping algorithm: a review. Optics Lasers Eng. 42, 245–261. https://doi.org/10.1016/j.optlaseng.2003.11.002.

Subramonian, S., Altan, T., Campbell, C., Ciocirlan, B., 2013. Determination of forces in high speed blanking using fem and experiments. J. Mater. Process. Technol. 213, 2184–2190. https://doi.org/10.1016/j.jmatprotec.2013.06.014.

Takahashi, T., Aoki, I., 1996. Development of analyzing system applicable for large plastic deformation. Proceedings 583–590.

Timmerbeil, F., 1957. Untersuchungen des Schneidvorganges bei Blech insbesondere beim geschlossenen Schnitt. Technische Hochschule Hannover Dissertation.

Vaz, M., Bressan, J.D., 2002. A computational approach to blanking processes. J. Mater. Process. Technol. 125–126, 206–212. https://doi.org/10.1016/S0924-0136(02)00313-8.

VDI-Fachbereich Produktionstechnik und Fertigungsverfahren, 1994. Schnittflächenqualität beim Schneiden, Beschneiden und Lochen von Werkstücken aus Metall; Scherschneiden. VDI-Handbuch Produktionstechnik und Fertigungsverfahren Band 2 VDI 2906 Blatt 2, 1–7.

Wang, K., Wierzbicki, T., 2015. Experimental and numerical study on the plane-strain blanking process on an ahss sheet. Int. J. Fract. 194, 19–36. https://doi.org/10.1007/s10704-015-0034-1.

Yamaguchi, I., 1981. Speckle displacement and decorrelation in the diffraction and image fields for small object deformation. Opt. Acta: Int. J. Optics 28, 1359–1376. https://doi.org/10.1080/713820454.